JOURNAL OF PROPULSION AND POWER
Vol. 25, No. 4, July–August 2009

Effect of Chamber Backpressure on Swirl Injector Fluid Mechanics

R. J. Kenny*
NASA Marshall Space Flight Center, Huntsville, Alabama 35812
James R. Hulka†
Jacobs Engineering, Huntsville, Alabama 35812
Marlow D. Moser‡
University of Alabama in Huntsville, Huntsville, Alabama 35812
and
Noah O. Rhys§
Yetispace, Inc., Huntsville, Alabama 35802

DOI: 10.2514/1.38537

Fluid mechanics of a liquid swirl injector element at various chamber backpressures were investigated. The center-jet swirling element was designed using typical liquid propellant rocket engine parameters, then manufactured and tested in a high-pressure, optically accessible, cold flow facility. Water was injected into a chamber pressurized with gaseous nitrogen at a constant swirl injector flow rate of 0.09 kg/s. The chamber backpressure ranged from 0.10 to 4.81 MPa. The film thickness and spray angle near the nozzle exit were measured by shadowgraphy. The film thickness was also measured within the injector upstream of the exit through a transparent nozzle tube section. Increasing the chamber backpressure for this fixed mass flow rate increased the film thickness from predicted design values. Measured discharge coefficient values increased with increasing chamber backpressure, reflecting the observed increase in internal nozzle film thickness. The spray angle decreased for increasing chamber backpressure.

Nomenclature

A	=	geometric parameter, $2D_nR_{\text{in}}/N_oD_o^2$
C_D	=	overall injector discharge coefficient
D_n	=	nozzle diameter
D_o	=	tangential orifice diameter
D_{vc}	=	vortex chamber diameter
L_n	=	nozzle length
L_o	=	tangential orifice length
L_{vc}	=	vortex chamber length
m_L	=	liquid mass flow rate
N_o	=	number of tangential orifices
P_c	=	chamber backpressure
P_{in}	=	supply pressure to injector element
R_{in}	=	radius from orifices to vortex chamber centerline
r	=	radial distance from nozzle centerline
t_n	=	film thickness
$t_{n,\text{avg}}$	=	spatially averaged film thickness between $2 < x/D_n < 4$
$t_{n,x/Dn}$	=	spatially averaged film thickness at a given nozzle cross section location, x/D_n
V_{ax}	=	axial velocity component of swirling liquid
V_{in}	=	tangential inlet velocity
V_{tang}	=	tangential velocity component of swirling liquid
V_Σ	=	total velocity magnitude
x	=	axial distance along nozzle length, referenced to the nozzle exit plane into the chamber
α	=	average nozzle area fullness coefficient, $1 - (1 - 2t_{n,\text{avg}}/D_n)^2$
β	=	vortex chamber to nozzle transition angle
ΔP	=	injector pressure drop
θ	=	free cone spray angle
ρ_L	=	liquid density
ζ_i	=	hydraulic flow loss coefficient

Received 13 May 2008; revision received 23 March 2009; accepted for publication 24 March 2009.

*Engineer, Acoustics and Stability Team, Mail Stop ER42. Member AIAA.
†Engineering Specialist, Engineering, Scientific, and Technical Services Group, Mail Stop ER32. Senior Member AIAA.
‡Associate Professor, Mechanical and Aerospace Engineering Department, Technology Hall S232. Senior Member AIAA.
§Senior Research Engineer. Member AIAA.

I. Introduction

SWIRL coaxial injection elements are commonly used within liquid propellant rocket engine injection systems. The coaxial element generally consists of a center post flowing liquid propellant. Upon exiting the center post, the liquid propellant is then sheared and atomized by the gas propellant flowing through a coaxially centered annulus. The liquid propellant is introduced into the center post through tangential slots at the post's top. Liquid tangential entry into the post imparts a swirling velocity component in conjunction with an axial velocity component. If the imparted tangential velocity component is high enough, then the liquid will separate along the post's centerline and an annular swirling flow is created with a finite film-thickness profile. This annular swirling flow moves axially down the post and exits into the engine chamber as a swirling sheet with a conical spreading angle, commonly known as the free cone spray angle [1]. The liquid separation inside the post causes a static pressure decrease along the post centerline which is subsequently filled with engine chamber gases.

The swirl coaxial element's center post, if designed well, can provide efficient propellant mixing and combustion flame stabilization. Film-thickness profile, the overall injector discharge coefficient, and the free cone spray angle are three basic spray features that guide swirl element center post design. The film-thickness profile, particularly the exit film thickness, provides the liquid inlet conditions for spray sheet formation in the engine chamber. The overall injector discharge coefficient rates how much pressure drop

the injection element is adding to the propulsion system's power balance. The free cone spray angle is related to how the injected liquid is spread and mixed with the shearing gas. Classic swirl element studies have focused chiefly on understanding basic spray feature relations with swirl element geometry, including analytical work by Bazarov et al. [1] and empirical work by Doumas and Laster [2]. Both studies provide explicit design relations between basic swirl element spray features and swirl injector element geometry but are anchored to experimental measurements at ambient backpressures. For liquid rocket engine operation, however, the swirl injection elements need to be designed for effective performance at elevated chamber backpressures. The effect of chamber backpressure on swirl element spray features is an area that has not been well developed and is consequently not incorporated into current swirl element design methodologies.

Dash et al. [3] measured swirl element film-thickness profiles at ambient backpressure and compared this profile to numerical predictions. Donjat et al. [4] imaged film-thickness profiles through transparent swirl elements flowing at ambient backpressure. It was experimentally observed that the internal swirling liquid surface displays helical wave structures, giving local film-thickness profiles variations along the axial centerline. Kim et al. [5] also imaged the internal film-thickness profiles and showed how unsteady the swirling flow was at ambient backpressure.

DeCorso and Kemeny [6], followed later by Ortman and Lefebvre [7], examined the influence of chamber backpressure on downstream spray angles and sheet distributions. Using radially oriented mechanical patternators, both works showed a general reduction of spray angle with increasing chamber backpressure up to 0.80 MPa. Both of these studies chose downstream measurement locations at axial distances greater than 10 nozzle diameters away from the nozzle tip, at which aerodynamic forces likely influence the spray shape. At such axial locations, the spray was assumed to be operating in the secondary atomization regime, where droplet fluid mechanics dictate spray behavior. This operating regime is much different than the near-tip regime of the spray where the design spray angle is located and the spray behavior is more closely linked to swirl injector element hydraulics. Recent work by Kim et al. [8] measured near-tip spray structure of spray angles and sheet breakup lengths as functions of Weber number and chamber-gas-to-liquid density ratio, at chamber backpressures up to 4.0 MPa. The spray angle increased as the Weber number increased. The spray angle was relatively insensitive to the density ratio changes until the intact sheet began to break up, where increases in density ratio decreased the spray angle. Unfortunately, none of these cited works measured injector discharge coefficient or internal film thickness along the nozzle.

In light of the aforementioned findings in the literature, a task was initiated with the objective to measure the effects of varying chamber backpressure on swirl injector fluid mechanics. Part of this task was to review previous research programs and associate what injector spray properties could be adequately captured in a nonreacting flow simulation. This review was accomplished by Kenny et al. [9], who identified important swirl injector spray features to be measured under varying chamber backpressures. The measurement of these important features was the main objective for the present work. Swirl injector features measured included internal film thickness within the nozzle, the injector mass flow rate discharge coefficient, and the total free cone spray angle. A single swirl injector element was designed and fabricated to allow for optical access of the internal nozzle flow. The swirl element was tested in an optically accessible, high chamber backpressure facility. The basic spray features were measured for a fixed mass flow rate and varying chamber backpressure. Nozzle internal film-thickness profiles and swirling sheet near-tip spray angles were measured using shadowgraphy. The overall injector discharge coefficient was also measured over the range of chamber backpressures tested. Comparisons were made between the measured spray features and the predicted spray values from available design methods. Spray atomization characteristics, such as mean droplet size and distribution, were not investigated in this work.

II. Experimental Hardware

A. Test Facility

A cross section of the water/nitrogen injector spray test (WNIST) chamber is shown in Fig. 1. Water is fed from a 0.13-m^3 run tank pressurized up to 9.93 MPa using a gaseous nitrogen (GN2) feed line, giving water mass flow rates up to 0.45 kg/s. The water flow rate was controlled in real time by a variable position valve (VPV), pneumatically actuated by gaseous nitrogen. After flowing through an installed injector, the water sprayed into a chamber pressurized by heated GN2 flowing across port windows mounted directly across from each other. The heated GN2 prevented most water from reaching the chamber windows and dried splatter. The GN2 was heated with a hot water heater system which kept the chamber gas temperature at approximately 300 K. The chamber backpressure could be regulated up to 9.65 MPa, but only 4.81 MPa was used for this work. The water and GN2 were vented through a set of exhaust VPVs located at the bottom of the chamber. The flow areas of the valves were set in conjunction with the window purge lines to maintain the desired chamber backpressure.

Static pressure and temperature measurements were recorded at 50 samples/s. The total uncertainties for each measurement (based on 95% confidence levels) were calculated using reported device calibrations, repeatability tests, and conventional uncertainty analysis methods [10]. Volumetric flow rates had a total uncertainty value of 4.4% of the nominal reading. Static pressure measurements had a maximum uncertainty of 114.6 kPa, and pressure difference measurements had a maximum uncertainty of 115.1 kPa. National Institute of Standards and Technology data tables were used to define the water and GN2 fluid properties of density, viscosity, and surface tension at constant temperatures in the chamber [11].

B. Swirl Injector Test Article

The swirl injector liquid mass flow rate of 0.09 kg/s was chosen to provide approximately 25 min of run time before the WNIST water supply tank emptied. The total free cone spray angle was selected to be a nominal value of 50 deg, narrow enough to reduce spray impingement on the chamber walls, but wide enough to image properly. The swirl injection element geometrical features were designed using the ideal design procedure by Bazarov et al. [1], and

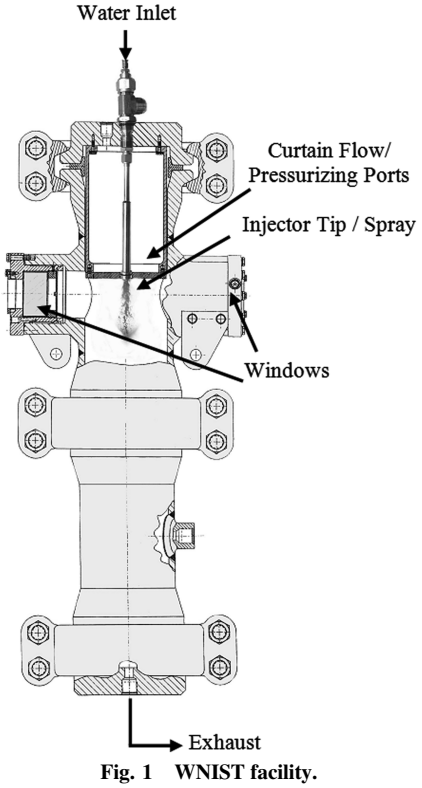

Fig. 1 WNIST facility.

Table 1 Element design values from Bazarov et al. [1] and Doumas and Laster [2] analyses

Design parameters	Intended	Bazarov et al. [1]	Doumas and Laster [2]
Mass flow rate, kg/s	0.09	0.09	0.09
Pressure drop, MPa	——	1.65	2.06
Free cone spray angle θ, deg	50	49.1	51.8
Tangential to axial velocity ratio, $\tan(\theta/2)$	0.47	0.46	0.49
Film thickness t_n, mm	——	0.43	0.40
Discharge coefficient, C_D	——	0.46	0.41
Total velocity magnitude V_Σ, m/s	——	57.49	48.03
Tangential orifice diameter D_o, mm	——	1.56	1.56
Tangential orifice length L_o, mm	——	3.73	N/A
Number of tangential orifices, N_o	3	3	3
Radius from orifices to swirl body centerline R_{in}, mm	——	1.61	1.61
Vortex chamber diameter D_{vc}, mm	——	4.78	4.78
Vortex chamber length L_{vc}, mm	——	3.93	N/A
Transition angle β, deg	118	118	118
Nozzle diameter D_n, mm	——	2.08	2.08
Nozzle length L_n, mm	——	3.12	N/A

the empirically based methodology by Doumas and Laster [2]. Swirl element parameters are listed in Table 1 and shown schematically in Fig. 2. The transition angle between the swirl chamber and nozzle was chosen to be 118 deg for simplification of machining. Doumas and Laster's correlations do not include lengths of the tangential orifices, the vortex chamber, or the nozzle, and so those dimensions were chosen using design recommendations by Bazarov et al. [1].

The injector consisted of three parts: a water manifold, a swirl body, and an acrylic nozzle extension. The water manifold was a cylindrical cavity into which water was delivered via stainless steel tubing. The cavity had an inner diameter to provide a radial water flow path into the swirl element orifices of at least $10D_o$. This radius promoted more one-dimensional flow distributions at the tangential orifice inlets. The swirl body was machined out of stainless steel hex bar stock. The hex design provided planar surfaces drilled directly for the three tangential orifices. Shown in Fig. 3 is the O-ring that seals the swirl body to the manifold.

Two different nozzle extensions, a cylindrical type and square type, were designed to provide optical access to the internal film-thickness profiles and downstream spray profiles. The cylindrical-type extension was a clear acrylic cylinder piece with a 50.8 mm diam and 14.4 mm length. A 2.1-mm-diam port was drilled through the cylinder's centerline. The nozzle diameter was confirmed to be 2.1 mm by placing a calibrated centering pin into the acrylic nozzle and verifying a tight fit. This cylindrical extension was geometrically aligned to the swirl body's exit plane using the calibrated pin so that the cylinder port was centered to the nozzle exit diameter of the swirl body. This successful alignment effectively extended the nozzle diameter by an additional 14.4 mm. This additional length was predicted to have little effect on the resulting film thickness and free cone spray angle based on work by Rahman [12]. The extension was bolted to the swirl body and sealed with an O-ring. To protect against strain from the bolt heads, a stainless steel cuff was placed against the bottom of the acrylic part. This extension type was used to image the internal nozzle film-thickness profiles. Because the outer diameter of the solid acrylic piece was so much greater than the inner post diameter, optical distortion through the acrylic was negligible and the section slightly magnified the flow moving down the inner post. However, optical distortion of the gas/liquid interface was important and was managed through techniques discussed later.

The acrylic square-type nozzle extension had the same overall length, O-ring seal, and drilled centerline port as the cylindrical type. The square-type extension had the same 50.8 mm diam as the cylindrical extension for approximately half of the overall length. Acrylic material was removed for the rest of the extension piece's length to form a square post. The widths of the square faces were double the drilled centerline port to provide for better imaging. Figure 4 shows the assembled manifold, swirler, and square-type acrylic section. This square-type nozzle extension was used when imaging the downstream spray profiles for spray angle

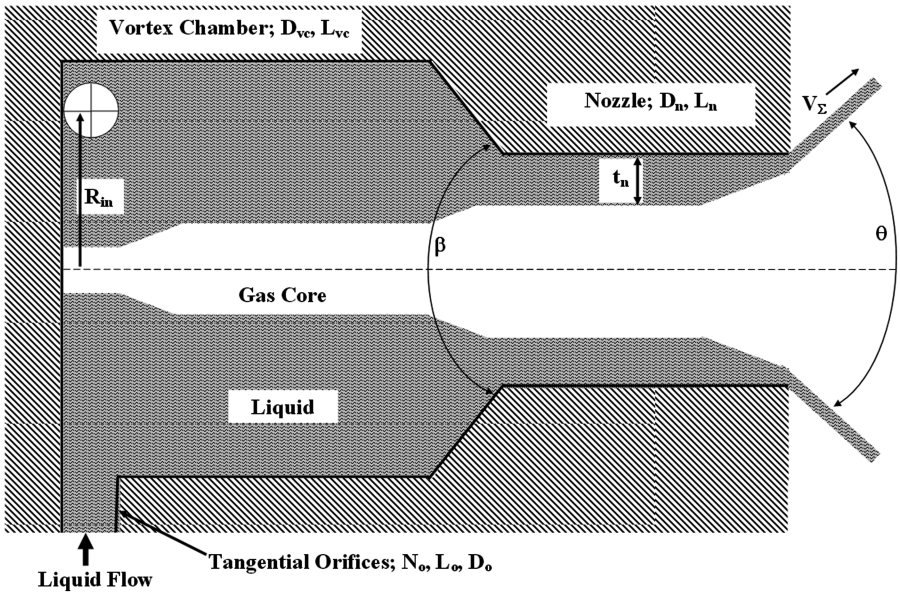

Fig. 2 Swirl injector geometry and fluid mechanic features (not to scale).

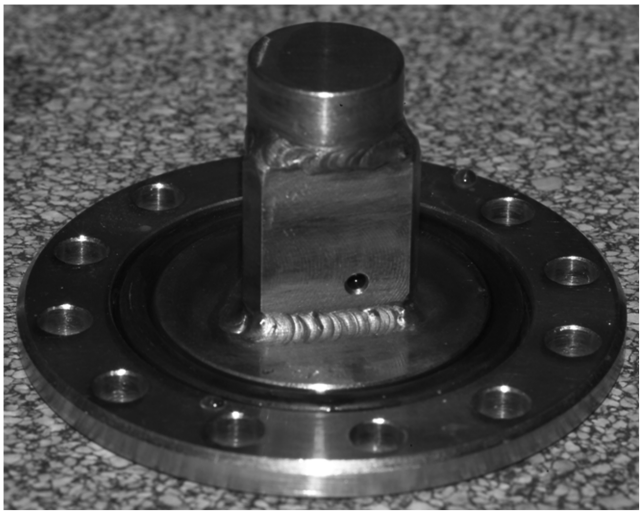

Fig. 3 Swirl element body.

a)

b)

Fig. 4 Assembled swirl element: a) profile view, and b) end view of acrylic section.

quantification. This extension type was used initially for film-thickness profile imaging, but the square profile distorted the light too much for reliable measurements.

C. Spray Feature Measurements

The spray features of interest were captured by shadowgraphy using a high-intensity strobe and a digital camera. A schematic of the shadowgraph setup is shown in Fig. 5. The light source was a model MVS-7010 high-intensity xenon strobe, made by the Machine Vision Corporation. Light-pulse duration was 20 μs per flash, with a maximum strobe frequency of 10 Hz. The strobe frequency was set at 1 Hz for short exposures or at 10 Hz for time-averaged pictures. Images were captured by a Kodak model DCS Pro/SLRn digital camera. This charge-coupled device camera took pictures at a 13.5 megapixel resolution, oriented as a 4500×3000 pixel grid [13]. Attached to the camera was a Nikon AF Micro-Nikkor telephoto lens, with a focal length of 200 mm and maximum aperture of four [13]. This telephoto lens provided increased resolution critical for focusing on key spray features. The camera was computer controlled to change camera settings and acquire images remotely during testing. Accepted images were adjusted to a horizontal reference and were converted to grayscale for further analysis.

To visualize unsteady flow, a high-speed video camera was used instead of the Kodak camera, and the strobe light was replaced by a 500 W steady halogen lamp. The high-speed video camera was a Phantom v7.3 from Vision Research, Inc. [14]. The frame resolution was set at 512×512 pixels, and the shutter speed was set for 10 μs. To increase picture resolution, the telephoto lens used for still camera pictures was used for the video captures as well. A frame rate of 4000 frames/s (fps) was selected after some evaluation to capture the majority of timescales observed during testing, while minimizing individual memory size. After 100 frames or 1/40th of a second were recorded, the video capture software saved the session to a multipage grayscale TIF (tagged image file) format.

Images were processed with ImageJ 1.37(c), created by Wayne Rasband under the National Institute of Health [15]. This image processing and analysis program was written in Javascript and has features such as image threshold settings, edge detection, pixel intensity histogram generation, and local zoom selection. Depending on the spray feature of interest, different tools of ImageJ were used to aid in the analysis and are discussed next.

III. Flow Diagnostics and Results

A. Discharge Coefficient

At ambient chamber backpressure, the measured injector pressure drop was 2.44 MPa at 0.09 kg/s, resulting in a 0.38 discharge coefficient. Bazarov et al.'s [1] inviscid theory predicted a lower value for injector pressure drop needed to supply the design mass flow rate, but flow loss effects are not included in Bazarov et al.'s method [1]. Conversely, Doumas and Laster's prediction showed better agreement to the measured pressure drop value, but it is grounded in measured data [2]. Figure 6 reports injector pressure drops needed to maintain the same mass flow rate of 0.09 kg/s at each chamber backpressure tested. These injector pressure drop values were normalized by the measured injector pressure drop at ambient chamber backpressure. Note that the injector pressure drop needed to maintain the same mass flow rate lowers with increasing chamber backpressure. The injector pressure drop values were used with the measured mass flow rate and nozzle exit diameter in Eq. (1) to calculate the discharge coefficient:

$$C_D = \frac{\dot{m}_L}{[(\pi/4)D_n^2]\sqrt{2\rho_L \Delta P}} \tag{1}$$

These discharge coefficient values are shown in Fig. 6. The total uncertainty of the discharge coefficients, determined using the measurement uncertainties values cited earlier, was 15% relative to the measured value. The injector pressure drop variable was the main contributor to the discharge coefficient uncertainty value.

Figure 6 shows that the measured discharge coefficient increased with increasing chamber backpressure. Bazarov et al. [1] have shown

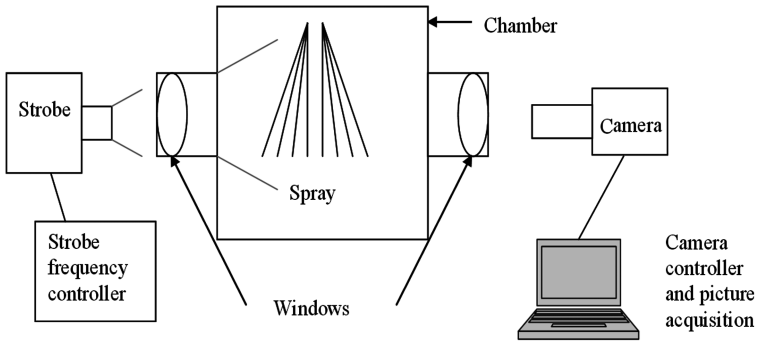

Fig. 5 Shadowgraph acquisition system.

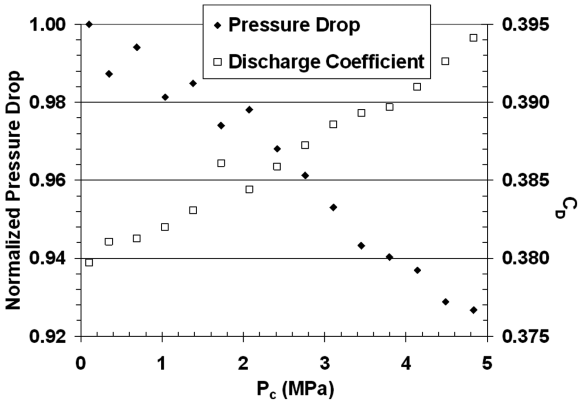

Fig. 6 Injector pressure drop and discharge coefficient variations with chamber backpressure.

that, for a fixed mass flow rate injector, increasing discharge coefficient values indicate that flow losses are increasing within the injector. Bazarov et al. have shown that flow losses within the swirling flow can be generally accommodated for by adding a flow loss term to the inviscid momentum relation [1]. The general momentum relation cited by Bazarov et al. to capture the swirling flow losses is given as Eq. (2):

$$\Delta P = \frac{\rho_L}{2}(V_{\text{ax}}^2 + V_{\tan g}^2 + \zeta_i V_{\text{in}}^2) \tag{2}$$

The hydraulic flow loss coefficient ζ_i is used to represent all flow losses occurring within the injector. Flow loss increase (e.g., from increased liquid viscosity) is represented by the flow loss coefficient increasing and the swirling flow's momentum decreasing for a fixed mass flow rate. Liquid flow tangential and axial velocity components will then decrease. Reduction in axial velocity will increase the liquid flow area in the injector and increase the average film thickness. Because the average film thickness and the injector discharge coefficient are directly related, increasing the film thickness will increase the discharge coefficient.

Several flow loss mechanisms can exist within the swirling flow. One flow loss mechanism that can be related to chamber backpressure changes is shearing friction at the gas/liquid interface. If the static gas density at the gas/liquid interface is assumed to be the same as that in the chamber, increasing chamber backpressure will increase the gas/liquid density ratio and the swirling liquid will lose momentum due to increasing shear friction losses [16]. The exact nature of how the increasing chamber backpressure is causing a flow loss to occur within the injector is a subject for future work.

B. Internal Flow High-Speed Imaging

After the operating conditions reached steady state within the injector element and chamber, the high-speed video camera filmed the swirling flow for 100 frames at 4000 fps. Each image session was cropped and magnified, but *not* scaled, into the region of interest along the swirler nozzle length. Except for a relatively small set of operating conditions that gave spatially unsteady behavior, the videos generally showed spatially stationary behavior of the internal nozzle flow. Therefore, the flow was deemed fairly time independent and digital high-resolution image stills could quantify internal flow features.

Figure 7 shows how the internal flow profiles changed with increasing chamber backpressure at the same mass flow rate of 0.09 kg/s. At atmospheric backpressure, the flow structure appeared helical. The helical flow structure came from liquid injection into the swirl chamber by three tangential slots, causing three main streamlines to form. Alignment of the three main streamlines created a helical pattern along the nozzle, with a flow profile showing striations in the direction of the swirling flow's helix angle. Bazarov et al.'s inviscid theory [1] predicts this helix angle to be 45.4 deg. The helical flow film thickness varied minimally due to turbulence, but generally remained constant over the duration of the video. As the chamber backpressure was increased to 0.34 MPa and 0.69 MPa, the same helical appearance was retained in the swirling flow. This helical pattern was similar to the helical patterns noted by Donjat et al. [4] and Kim et al. [5], but how the helical streamlines were distributed down the nozzle axis or how the streamlines were related to exiting spray sheet characteristics were not further investigated in this work.

At 1.03 MPa, the swirling flow began to show asymmetric variations in its profile, of which a portion with a thicker film (or smaller air core diameter) is marked in Fig. 7 as a "neck." The location of this neck was centered roughly two-thirds of the nozzle length down from the bottom of the O-ring groove between the swirl body and the acrylic nozzle, and moved randomly about this point approximately ± 2 mm. Flow upstream and downstream of the neck location maintained the same helical flow morphology and film thicknesses as at ambient backpressure. Increasing the chamber backpressure to 1.37 MPa moved the neck further upstream to roughly half of the nozzle length, with the same random variations and film thicknesses upstream and downstream of the neck as measured at ambient backpressure.

At 1.72 MPa, the neck moved further upstream from the nozzle exit and the film thickness at the neck increased. The flow upstream of the neck maintained the same film-thickness profile as at ambient backpressure, but the flow downstream of the neck was distorted and film thickness increased. Also, a second neck appeared that did not have the same appearance as the first neck. Both necks were spatially stationary in time. For clarification, if a flow neck had no perceivable film-thickness profile distortions upstream, this neck was labeled a "jump." For the 1.72 MPa image in Fig. 7, the flow jump is distinguished by a left-side arrow. The film-thickness profile upstream of the jump is visually similar to the profile seen for 0.10 MPa. The second neck is located further downstream and is denoted by a right-side arrow. Flow necks always follow after the first flow jump and have changes in film-thickness profiles both upstream and downstream of the neck location.

Increasing the chamber backpressure to 2.06, 2.41, and 2.76 MPa moved the initial upstream jump location toward the swirl chamber of the injector, and one to two downstream necks were formed in the

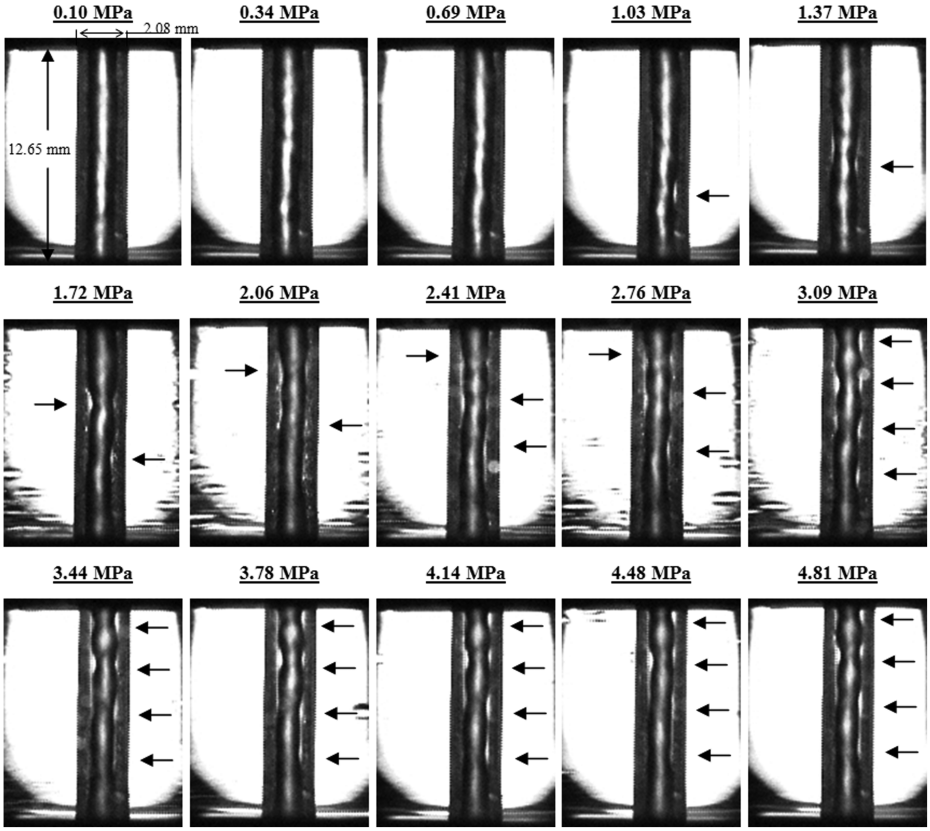

Fig. 7 Internal swirling flow profiles at the design mass flow rate and various back pressures. Images are frames from high-speed video captures. Arrows on the left side denote jumps, arrows on the right side denote necks.

flow. The location of the upstream jump and downstream necks stayed spatially stationary. However, in addition to the changes in film thickness due to jump and necks, the film thickness downstream of the jump increased.

For 3.09–4.81 MPa, the flow profile no longer had a visually notable upstream jump. It was assumed that the jump had moved upstream out of the viewable nozzle length. Multiple necks (three to four) were noticed along the nozzle length, and the location of these necks did not greatly vary with increasing backpressure. The film along the nozzle was the thickest seen over the chamber backpressure range investigated.

Observations from Fig. 7 implied that the increasing chamber backpressure strongly influenced the internal gas core behavior of the swirling flow. This observation was in tandem with the changes in discharge coefficient plotted in Fig. 6. Note that the discharge coefficient data point at $P_c = 1.72$ MPa is out of trend with the other data points. This data point coincides with the first observation of a jump inside the injector. It was assumed that, when the chamber backpressure was increased enough, the interface friction losses incited a change in the swirling flow state. This change in liquid flow state is analogous to changes in gas flow states seen within Fanno flow [16].

C. Film-Thickness Measurements

During a given operating condition, the camera and optically accessible section of the swirler were oriented so that the entire vertical length of the nozzle was captured. The swirling flow appeared asymmetric halfway down the optical nozzle length. This asymmetry was noted as being constant for all mass flow rates at atmospheric conditions, and so it was hypothesized that the swirler nozzle had some slight internal surface imperfections along the internal nozzle surface. These imperfections, however slight, come from the nozzle machining process, and cause a spatially stationary "curving" of the flow. The flow asymmetry could also have been part of the flow character itself, as has been seen in internal flow images captured by Donjat et al. [4]. The flow asymmetry was considered part of the nominal imaged flow, and its effects on film-thickness

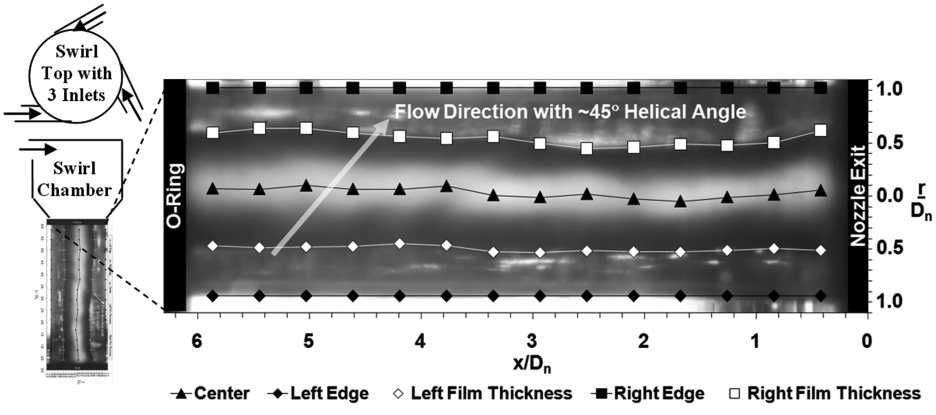

Fig. 8 Film-thickness profile measurements for ambient chamber backpressure.

estimation were averaged out through the process described next. This asymmetry can be seen in Fig. 8.

The film thickness along the optical nozzle length was measured by determining the pixel-based values from still images. Fourteen axial locations along the nozzle length were selected to measure film thickness. For an average film-thickness measurement, ImageJ's rectangular selection feature was used to select a 50-pixel-high region per axial location [15]. This selection contained multiple rows of line selections with individual intensity values. ImageJ was used to take the spatial average of each pixel row within the rectangular selection, giving composite average pixel intensity values versus horizontal pixel location. The measured intensity curves were replaced with smoothed curves generated using a five-point median processing technique.

The intensity profile versus pixel location defined the four features needed to determine average film thickness: the leftmost nozzle diameter edge, the left edge of the liquid film/gas interface, the right edge of the liquid film/gas interface, and the rightmost nozzle diameter edge. The intensity derivative was either a minimum or a maximum at locations where the nozzle diameter edge distorted the background light. For the left nozzle edge, the intensity changed from high to low, denoting a large negative derivative. For the right nozzle edge, the intensity changed from low to high, denoting a large positive derivative. Thus, the intensity versus pixel location relationship was differentiated, and the derivatives plotted to determine the most negative and positive values. The subsequent pixel values at these high derivatives were then recorded as the left and right reference edges of the nozzle diameter. Smoothed curves helped suppress measurement noise amplified in the derivative curves and aided in determining the best zero-crossing of the derivative.

The last step in determining the film thickness from the mean intensity values consisted of recording, for each chamber backpressure value, the four pixel locations corresponding to the left-side nozzle diameter edge, the left-side gas/liquid interface, the right-side gas/liquid interface, and the right-side nozzle diameter edge. The difference between the nozzle diameter edges and the gas/liquid interfaces was the film thicknesses for each side. The pixel-to-length ratio was defined from the difference between the left- and right-side nozzle diameter edges corresponding to the known value of nozzle diameter. The pixel-to-length conversion, defined as the nozzle diameter length divided by the pixel width across the imaged nozzle diameter, was found to be 0.0061 mm/pixel. This pixel-to-length conversion was checked and verified against other reference lengths (i.e., injector bolt head diameters) imaged with the same camera settings. This conversion factor also accommodated for the flow magnification noted in Sec. II.B.

The accuracy of this pixel-based film-thickness process was determined to be a summation of two biases: the bias due to nozzle diameter edge resolution and the bias due to the gas/liquid interface edge resolution. The total pixel-based film-thickness bias has a composite bias of ± 2 pixels, which corresponded to a length bias of ± 0.008 mm. Repeated measurements of the same images gave a repeatability of ± 3 pixels and an average film-thickness repeatability of ± 0.013 mm. Combining the bias and repeatability measurements [10], the total uncertainty of the average film thickness was defined as ± 0.015 mm. No other film-thickness measurement techniques were available during this work for comparison with the image processing technique described earlier.

Previous work performed by Binnie [17] investigated swirling water flow moving down a clear plastic tube, which allowed for air entrainment into the vortex core. Background illumination was used to highlight flow features during photography. Binnie noted that refraction effects at the gas/liquid interface could distort the visually perceived edges of the swirling flow [17]. Optical correction methods were developed and simplified to correct for these effects.

The refraction correction method stipulated certain criteria on the ratio of the nozzle diameter to the outer plastic diameter, as well as the viewing angle of the camera. The criteria Binnie [17] specified were 1) the camera/lighting setup had to be vertically level with the acrylic section, and 2) the center of the gas core had to be vertically centered with the background lighting. Because the acrylic nozzle geometry and experimental setup in the current study satisfied both of Binnie's refraction correction criteria, Binnie's correction method was deemed viable for use with these data. Through Snell's law, the physical gas core radius (or the nozzle radius less the film thickness) is the visually determined gas core radius divided by the index of refraction of water, 1.33 [18]. For each flow condition, the measured left and right film thicknesses were divided by the index of refraction for water to give the corrected values, as shown in Fig. 8. Values are reported in radial locations referenced to the nozzle radius and axial spatial location along the nozzle length relative to the nozzle diameter.

Comparison between the left and right film thicknesses in Fig. 8 show that they are notably different, partly due to the asymmetry of the helical flow. The left and right film-thickness profiles are plotted in Fig. 9 versus a subset of each chamber backpressure examined. The axial asymmetry between the two plots highlight the effect of the helical pattern of the flow on measured film-thickness values at any given axial location.

Doumas and Laster empirically determined the film thickness by optical measurement of the air core diameter [2]. Because of line-of-sight limitations, this method thus measures a minimum gas core diameter or a maximum film thickness. Bazarov et al.'s [1] relations assume a constant average film thickness along most of the nozzle length and an exit film thickness at the nozzle exit. Neither Bazarov et al. [1] nor Doumas and Laster [2] provide any description of the spatial distribution of the film thickness along the nozzle. To compare the measurements from this work to both design methods, the two film-thickness profiles from Fig. 9 were averaged per spatial location and chamber backpressure. The results, along with the predicted film-thickness values, are shown in Fig. 10. Predicted exit

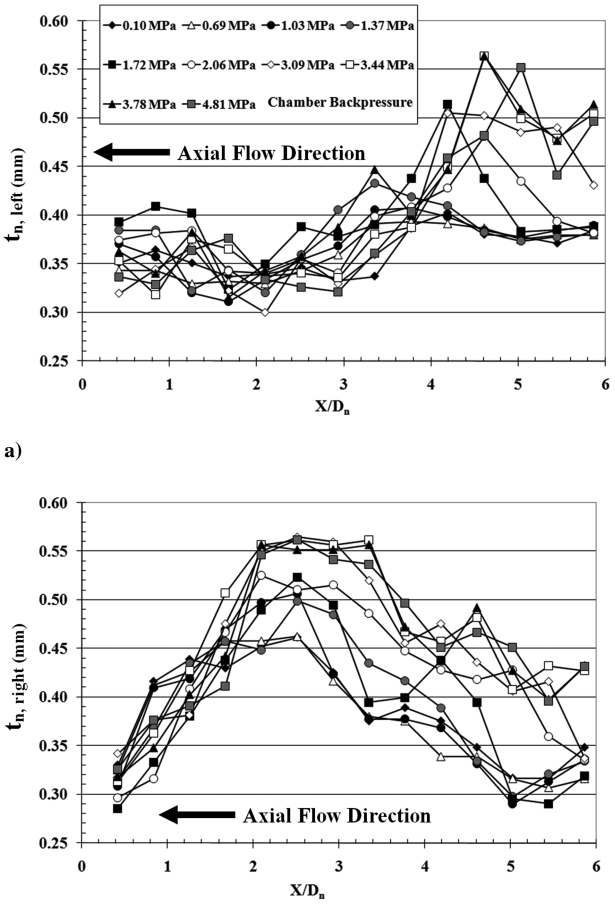

Fig. 9 Comparison between a) left and b) right film-thickness profiles over various chamber backpressures.

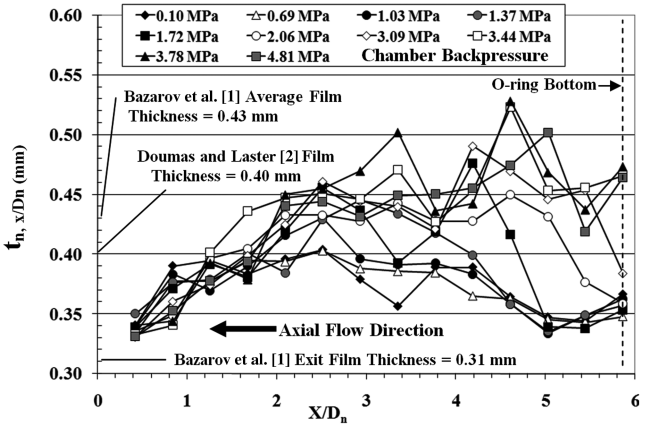

Fig. 10 Film-thickness profile measurements at various chamber backpressures.

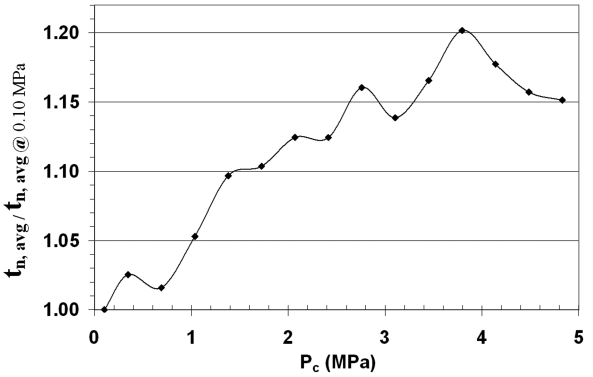

Fig. 11 Spatially averaged film-thickness profile measurements.

film thicknesses, using Bazarov et al.'s methodology [1], were the same value of 0.31 mm for all chamber backpressures.

Figure 10 shows the maximum film-thickness value generally increasing with increasing chamber backpressure. The highest maximum film thickness was measured approximately 4.5 nozzle diameters upstream of the nozzle exit plane for a chamber backpressure of 3.78 MPa. The three spatial locations closest to the nozzle exit showed little change to variations in chamber backpressure. Hutt previously noted a similar behavior of film-thickness spatial variation along the nozzle length [19]. Although the independent variables in Hutt's work were the swirler inlet geometries, the measured exit film thicknesses showed little change over a variety of different configurations. Hutt also noted that the film-thickness variance could be due to a flow instability mechanism, which could set up a long wavelength variation along the nozzle. The film-thickness values in Fig. 10 decrease as one approaches the nozzle exit plane. The film-thickness values seem to approach Bazarov et al.'s methodology-predicted exit film-thickness value [1].

To best compare with 1-D method predictions of film thickness, two different representative film-thickness values from Fig. 10 were calculated: 1) an axially averaged film thickness determined over the normalized nozzle length of 2–4 nozzle exit diameters, and 2) the film-thickness values reported at a normalized nozzle length of 0.42 nozzle exit diameters. The axially averaged film-thickness value was calculated to compare with the Bazarov et al.'s prediction [1]. The film-thickness values at $X/D_n = 0.42$ were calculated to observe how the near-exit film-thickness values changed with chamber backpressure. The Doumas and Laster prediction of maximum film thickness was approximately -1.5% relative to the maximum local film-thickness value at ambient chamber backpressure [2]. Bazarov et al.'s film-thickness prediction was 13% higher than the average film-thickness value at ambient chamber backpressure, due to inviscid flow assumptions [1], which generated a higher liquid flow area within the nozzle.

Figure 11 shows the observed increase in spatially averaged film thickness with chamber backpressure. Film thickness values are normalized against the axially averaged film-thickness value at 0.10 MPa. Increasing film-thickness values correlated well with the increasing discharge coefficient values in Fig. 6, reaffirming the influence of increasing internal flow losses. Figure 12 shows the results of the other two calculations, which showed the near-exit film-thickness values' relative insensitivity to backpressure. Values are normalized to the near-exit film-thickness values at 0.10 MPa.

D. Spray Angle

Measurement of the free cone spray angle required quantification of the spray sheet boundary profile. Because the spray displayed unsteady motion, high-speed digital video was used to capture time-dependent images. The high-speed video setup was the same as shown in Fig. 5. The operating conditions during spray filming were the same as studied for the film thickness. The swirl injector configuration tested was the same as used in the previous discussions, with the cylindrical extension replaced with the square-type extension. Typical single frames from each video capture session are shown in Fig. 13. The frames in Fig. 13 were downgraded in quality for viewing purposes only; the original frame quality was deemed high enough for accurate spray angle estimation.

Once mass flow rates and chamber backpressures displayed steady values, the issuing spray was captured for 300 sample frames. The video captures showed multiple undulations of the spray boundary within the capture period. The 75-ms video time provided an adequate representation of the spray, based on an injection velocity of 50.7 m/s calculated from Doumas and Laster [2] and a region of interest within the capture frame of six nozzle diameters downstream of the nozzle exit plane. Using this representative length scale and the total velocity, the travel distance for a fluid element to move downstream 6 nozzle diameters was 0.25 ms. A 75-ms capture time gave 300 "convection periods" of the spray, yielding an acceptable number of periods for averaging.

Figure 14 shows a representative session frame from a captured video of the spray at ambient chamber backpressure and mass flow rate of 0.09 kg/s. The nozzle diameter width, the exit plane, and the spray angle are all demarcated in the figure. Spray angles were measured close to the nozzle exit to document the evolving profile of the spray boundary, as well as to define the most relevant spray angle of the nonreacting fluid mechanics directly related to the swirl element design [9]. Spray angle measurements were taken at nine locations ($0.25D_n$, $0.5D_n$, $0.75D_n$, $1D_n$, $2D_n$, $3D_n$, $4D_n$, $5D_n$, and $6D_n$) downstream of the nozzle exit plane. The tighter spacing between measurement locations upstream of 1 exit diameter was chosen because the spray was observed to have notable changes of boundary shape in that region. Downstream of 1 exit diameter, the spray boundary varied more linearly, and so a wider spacing was used. Spray angles upstream of 1 nozzle diameter are not reported because the total measurement uncertainties at those locations were excessive.

The free cone spray angle was measured in several steps. An example spray boundary capture process is as follows. The issuing

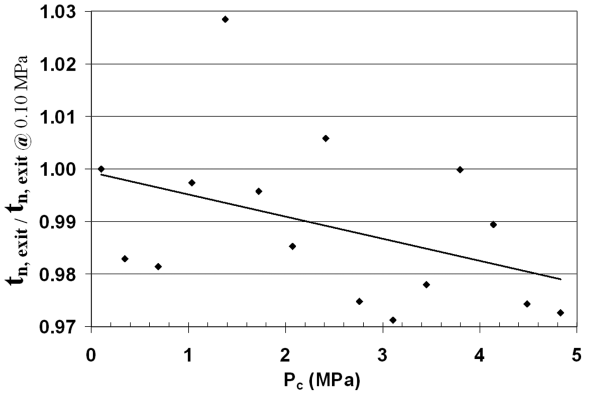

Fig. 12 Exit film-thickness profile measurements at $X/D_n = 0.42$.

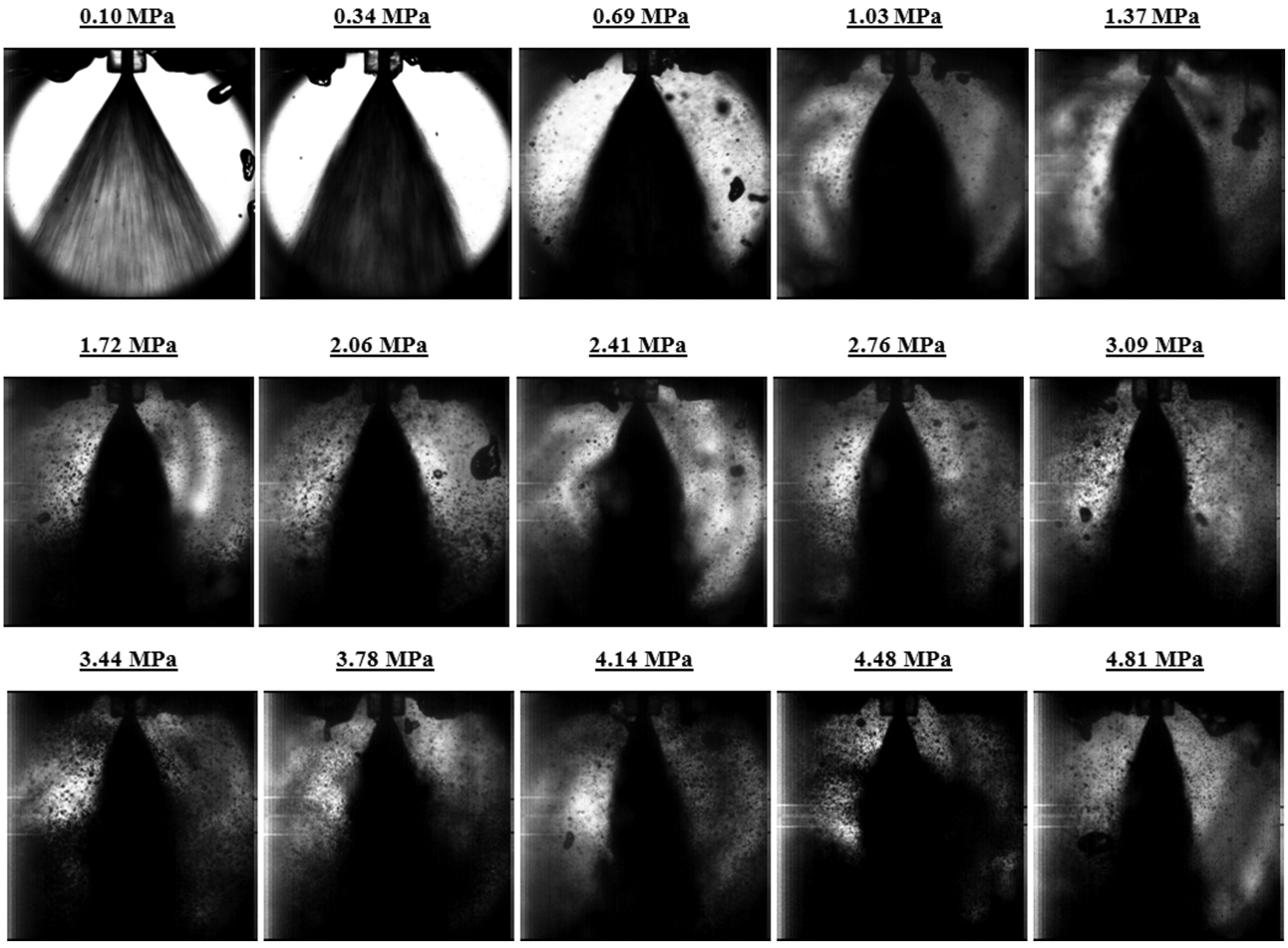

Fig. 13 Spray profiles at the design mass flow rate and various chamber backpressures.

spray was captured using the Phantom video camera in conjunction with the Phantom Cine Control Panel software [14]. From the captured frameset, a representative 100 sequential frames were chosen by finding the best time period where the spray was discernible. The representative frameset was saved as a multipage TIF file to best preserve image resolution.

Postprocessing of the images established accurate spray boundary contrasts using a repeatable method for each processed image. First, the mean pixel intensity was determined to convert the TIF file from a grayscale format to a binary black/white format. Next, spurious droplets in the captured flowfield near the spray boundary were deemphasized by removing pixels from the edges of black objects within the image, and adding pixels back to the black edges, which smoothed black objects within binary images and removed isolated pixels in the images. Figure 15 compares an unprocessed image with the corresponding postprocessed image.

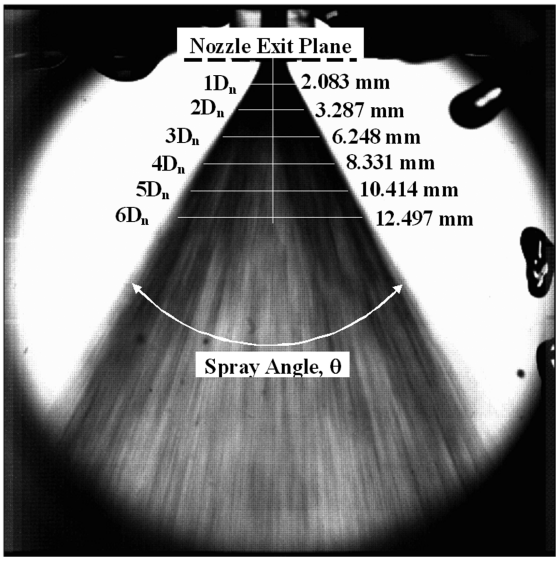

Fig. 14 Spray boundary measurement locations.

Next, pixels of interest at the downstream locations were tagged and the intensity associated for each tagged pixel for each frame was measured. Pixel intensities were then grouped to individual pixel locations and the mean intensity value for each pixel location was calculated by averaging over all 100 frames. The mean intensity for each pixel location was then collimated for each downstream location. Finally, for each downstream location, the central difference numerical derivative was calculated by an automated software routine, giving the intensity gradient at each pixel location. Spray boundary edges were determined numerically by large derivative values. An alternative edge detection method was tried by finding, for each downstream location, the "first" black pixel seen at the sheet boundary. Because this alternative method gave higher error, because the first black pixel could be a spurious black droplet separated from the spray boundary and not the actual spray boundary itself, it was abandoned. Comparisons of spray boundaries for the images in Fig. 15 are shown in Fig. 16. Estimates of the spray boundaries were made for several chamber backpressures by visually discerning the spray boundary for multiple frames. These visual estimates compared well to the automated method's estimates for spray boundary values 1 nozzle diameter and greater downstream of the nozzle exit plane.

The local spray angles at the left and right sides of each downstream location were measured once the spray boundary was defined. The spray boundary spray angles were calculated with respect to the 2-D spatial locations of the left and right edges of the nozzle exit

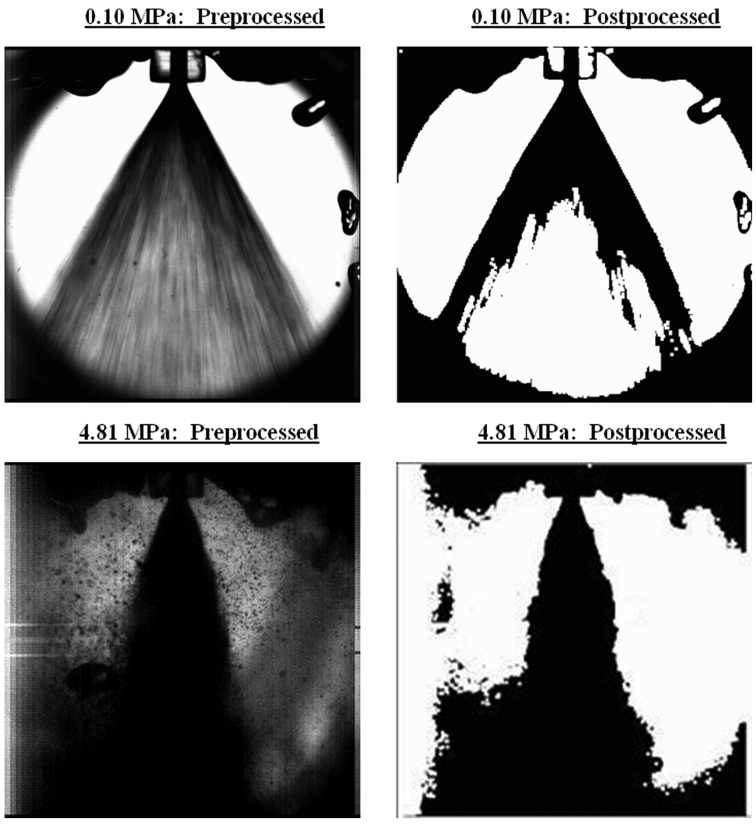

Fig. 15 Effect of image postprocessing to the captured images for two chamber backpressures.

diameter. The total spray angle for each downstream location was the sum of the left and right results. The spray boundary was resolved to within ± 1 pixel, which corresponded to a total spray angle uncertainty of ± 2 deg. The free cone spray angle was defined as the local spray angle, measured at the spray boundary inflection point. The local spray angle at the inflection point was the largest possible angle, assuming no other secondary flow effects disturbed the issuing spray. The free cone spray angle was selected at each operating condition by choosing the largest local spray angle value over all of the downstream locations.

Figure 17 compares the measured free cone spray angles for a fixed mass flow rate and varying chamber backpressure. The downstream location corresponding to free cone spray angle measurement ranged over 2–6 nozzle diameters. The plotted error bars represent the specified uncertainty bands. With these error bars included per measurement, comparison of the predicted free cone spray angle from Doumas and Laster [2] show good agreement at ambient chamber backpressure. In accordance with the higher predicted discharge coefficient and average film thickness, the predicted free cone spray angle from Bazarov et al.'s method was lower than the measured values at ambient conditions [1].

Figure 17 shows that the measured spray angle generally decreases linearly with increasing chamber backpressure. This linear trend is represented by a straight line fit through the data plotted in Fig. 17. The spray angle measurements seem to follow this straight line fit except for the last data point at a chamber backpressure of 4.81 MPa. This data point was kept in Fig. 17 with the rest of the spray angle measurements because the measurement procedure was the same for all data points, giving no reason to omit this measurement on the basis of anomalous data.

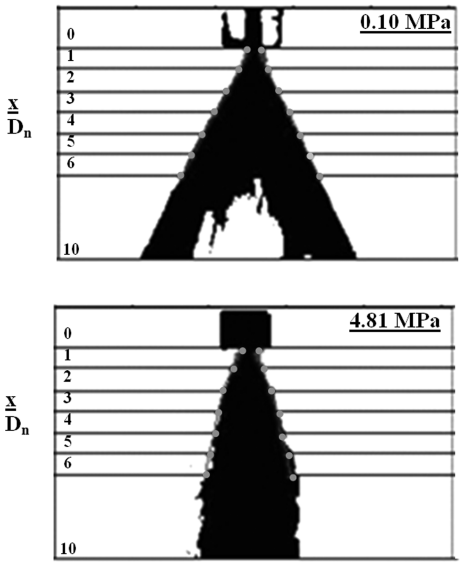

Fig. 16 Comparison of spray boundary measurements to a single frame at different chamber backpressures. Gray dotted lines indicate boundary measured from image processing.

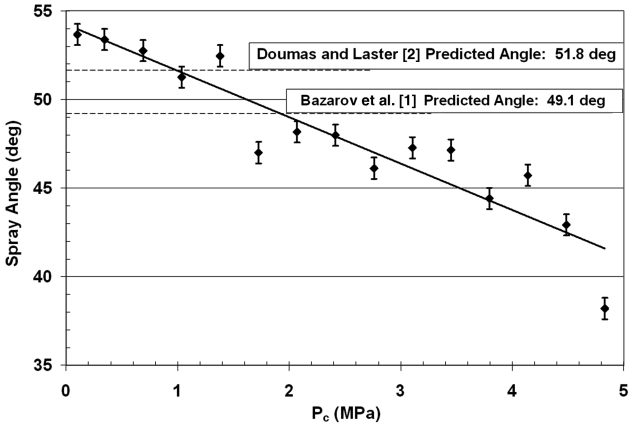

Fig. 17 Free cone spray angle values for varying chamber backpressures.

An explanation is offered for this anomalous point. For low-to-moderate chamber backpressure values, the spray's breakup length could be located at downstream distances of greater than 6 nozzle diameters. Measured spray angles in Fig. 17 are then representative of intact sheet hydraulic angles and not of atomization zone angles. If the spray's primary atomization zone has steadily moved closer to the injector tip as the chamber backpressure is increased, then the measured spray angle becomes representative of atomization zone angles. Results produced by DeCorso and Kemeny show atomization zone angles would likely show more decrease with increasing chamber backpressure than for lower chamber backpressures [6]. It is possible that the spray is breaking up into the atomization regime close to the nozzle exit plane, which would change how the measured spray angle trends are interpreted. Explanations for how the hydraulic spray angle and atomization zone spray angles change with increasing chamber backpressure are given next.

1. Hydraulic Spray Angle

Figure 17 displays a clear trend of decreasing free cone spray angles with increasing chamber backpressure. Trends shown in Figs. 6, 11, and 17 agree well with the general trend of increasing swirl element losses proposed by Bazarov et al. [1]. Increasing the chamber backpressure increased the apparent flow losses experienced by the swirling liquid, lowering the liquid momentum and increasing the injector discharge coefficient. This loss of liquid momentum also caused the average film thickness to increase and the subsequent free cone spray angle to decrease.

Bazarov et al. suggested that injector losses can be accounted for within inviscid swirl design relations by recalculating the geometric parameter A, using one or more measured injector properties [1]. This "equivalent" geometric parameter A_{eq} can then be used to make an updated prediction of the free cone spray angle. Unnormalized film-thickness values in Fig. 11 were used to calculate an average fullness coefficient α. A_{eq} was then calculated from the average fullness coefficient values at each chamber backpressure. The calculated average fullness coefficient values were then plotted against the measured spray angles previously shown in Fig. 17. These values are shown in Fig. 18. Note that the spray angles are represented as tangent of half the spray angle values. This conversion was used to give a better indication of how the ratio between the tangential and axial liquid velocity components changed with increasing chamber backpressure.

Both the Bazarov et al. [1] and Doumas and Laster [2] design methods use the geometric parameter to give a direct link between the measured average fullness coefficient and the predicted free cone spray angle. Both methods were used to predict the free cone spray angle over the range $0.6 < \alpha < 0.7$ to compare with the measured spray angle values. Both methods agree that increasing α will decrease the injected free cone spray angle. The predictions show a linear relationship between α and the spray half-angle tangent which

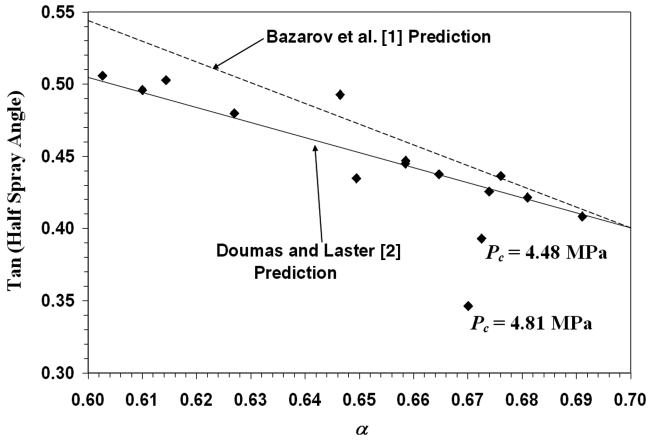

Fig. 18 Measured α vs tangent of measured spray half-angle. Also plotted are the predicted Bazarov et al. [1] and Doumas and Laster [2] spray angles using the measured range of α.

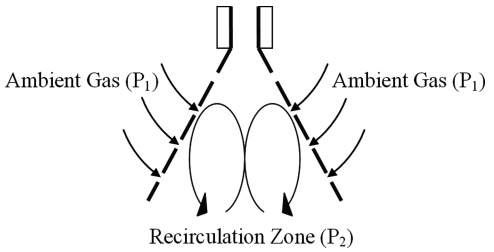

Fig. 19 Schematic of liquid swirl sheet-induced recirculation and the motion of the ambient gas. Ambient gas flow is promoted through the spray boundary since $P_1 > P_2$.

is similar to the data trend for all values except at $P_c = 4.81$ MPa. This value corresponds to the anomalous point noted in Fig. 17 and is possibly not representative of a hydraulic spray angle at this higher chamber backpressure. For higher chamber backpressures, the spray angle is more representative of an atomization zone spray angle, described in the next section.

2. Atomization Zone Spray Angle

As the spray continues downstream from the injector exit plane, the intact liquid sheet will breakup and disintegrate into a droplet cloud whose behavior is dictated by droplet spray mechanics and not intact sheet mechanics. DeCorso and Kemeny [6] gave an explanation of how chamber backpressure influences spray angles created in the spray's atomization zone. The spray issues out into the chamber and creates a conical sheet, which has vortex recirculation zones created within the volume bounded by the sheet. These vortices create a low static pressure region in the sheet-bounded volume, promoting gas flow from outside the spray boundary toward the volume. This gas flow contracts the liquid spray boundary and can increase the spray's primary and secondary atomization zones by decreasing the spray's breakup length. A spray boundary still exists, but is now defined by a droplet cloud sheath instead of an intact sheet. Figure 19 shows graphically how the pressure differences contract the spray boundary. Spray boundary reduction for a droplet cloud sheath is greater than intact sheet boundary reduction because the drag effect on the droplets is greater. The droplets are better entrained toward the flow's axial centerline, providing a smaller apparent spray angle.

Axial locations of the radial patternators used in DeCorso and Kemeny's studies were at least 40 nozzle exit diameters away from the injector tips [6]. These axial distances are much further away from the injector exit plane than those measured in this work. Thus, trends previously observed in a spray angle with chamber backpressure are likely different from the measurements in the current study. Direct comparison between the spray angle measurements of this work and the results reported by DeCorso and Kemeny were deemed inappropriate and were not performed.

IV. Conclusions

In an effort to quantify the effects of chamber backpressure on swirl injector element fluid mechanics, a swirl element was designed, fabricated, and tested at elevated chamber backpressures with water as the working fluid. Shadowgraphs of the optically accessible nozzle showed that increasing chamber backpressure produced necking of the average film-thickness profiles. The necks varied in size and location based on the chamber backpressure value, but were mostly spatially stationary along the nozzle length. By spatially averaging along the measured film-thickness profiles, it was shown that increasing the chamber backpressure increased the average film thickness at a fixed mass flow rate. This general trend was attributed to increased liquid momentum losses due to gas/liquid interfacial shear driven by the increasing gas density. Increasing momentum losses also caused the mass flow discharge coefficient to increase with chamber backpressure. This discharge coefficient increase was due to the average film thickness increasing from reduction in liquid velocity component values for a fixed mass flow rate.

Using high-speed videography, downstream spray boundaries were captured over the chamber backpressure values tested. Analysis of the video captures gave free cone spray angle definition at each backpressure value in the near-tip region of the spray. In general, the increase in chamber backpressure decreased the free cone spray angle. This trend of decreasing spray angle was in concurrence with the trend of increasing average film thickness and discharge coefficient. The amount of spray angle decrease with backpressure was less in comparison with previous works, but although this work measured near-tip spray angles, previous works measured spray angles far downstream of the nozzle exit plane. At these far distances, droplet behavior, not sheet behavior, govern the fluid mechanics and the spray angles.

Acknowledgments

This work was funded under NASA's Constellation University Institutes Project, directed by Claudia Meyer and Jeff Rybak. Facility support was reliably provided by the personnel of NASA Marshall Space Flight Center's East Test Area. Nick Hensley provided excellent support during testing.

References

[1] Bazarov, V., Yang, V., and Puri, P., "Design and Dynamics of Jet and Swirl Injectors," *Liquid Rocket Thrust Chambers: Aspects of Modeling, Analysis, and Design*, edited by V. Yang, M. Habiballah, J. Hulka, and M. Poppe, Vol. 200, Progress in Astronautics and Aeronautics, AIAA, Reston, VA, 2004, pp. 19–103.

[2] Doumas, M., and Laster, R., "Liquid-Film Properties in Centrifugal Spray Nozzles," *Chemical Engineering Progress*, Vol. 49, No. 9, Oct. 1953, pp. 518–526.

[3] Dash, S. K., Halder, M. R., Peric, M., and Som, S. K., "Formation of Air Core in Nozzles with Tangential Entry," *Journal of Fluids Engineering*, Vol. 123, No. 4, Dec. 2001, pp. 829–835. doi:10.1115/1.1412845

[4] Donjat, D., Estivalezes, J., Michau, M., and Lavergne, G., "Phenomenological Study of the Pressure Swirl Atomizer Internal Flow," *Proceedings of the 9th International Conference on Liquid Atomization and Spray Systems*, 2003, pp. 12–19.

[5] Kim, S., Kim, D., Khil, T., and Yoon, Y., "Effect of Geometry on the Liquid Film Thickness and Formation of Air Core in a Swirl Injector," AIAA Paper No. 2007-5460, July 2007.

[6] DeCorso, S. M., and Kemeny, G. A., "Effect of Ambient and Fuel Pressure on Nozzle Spray Angle," American Society of Mechanical Engineers Paper No. 1956-GTP-3, April 1956.

[7] Ortman, J., and Lefebvre, A. H., "Internal Fuel Distributions from Pressure-Swirl Atomizers," *Journal of Propulsion and Power*, Vol. 1, No. 1, 1985, pp. 11–15. doi:10.2514/3.22752

[8] Kim, D., Im, J., Koh, H., and Yoon, Y., "Effects of Ambient Gas Density on Spray Characteristics of Swirling Liquid Sheets," *Journal of Propulsion and Power*, Vol. 23, No. 3, 2007, pp. 603–611. doi:10.2514/1.20161

[9] Kenny, R. J., Moser, M. D., Hulka, J. R., and Jones, G., "Cold Flow Testing for Liquid Propellant Rocket Injector Scaling and Throttling," AIAA Paper No. 2006-4705, July 2006.

[10] Coleman, H. W., and Steele, W. G., *Experimentation and Uncertainty Analysis for Engineers*, 2nd ed., Wiley, New York, 1999.

[11] Lemmon, E. W., McLinden, M. O., and Friend, D. G., "Thermophysical Properties of Fluid Systems," *NIST Chemistry WebBook, National Inst. of Standards and Technology Standard Reference Database No. 69*, edited by P. J. Linstrom, and W. G. Mallard, National Inst. of Standards and Technology, Gaithersburg, MD, June 2005, http://webbook.nist.gov.

[12] Rahman, S. A., "Primary Atomization Study of a Swirl Coaxial Liquid Propellant Rocket Injector," Ph.D. Dissertation, Dept. of Mechanical Engineering, Pennsylvania State Univ., University Park, PA, 1997.

[13] "Kodak Professional DCS Pro SLR/n Digital Camera User's Guide," Eastman Kodak Co., Rochester, NY, 2004.

[14] "Phantom v7.3 Datasheet," Vision Research, Inc., Wayne, NJ, Oct. 2007.

[15] Rasband, W. S., ImageJ, U.S. National Inst. of Health, Betheseda, MD, 1997–2007, http://rsb.info.nih.gov/ij/.

[16] White, F. M., *Fluid Mechanics*, 4th ed., McGraw–Hill, New York, 1999.

[17] Binnie, A. M., "Annular Hydraulic Jumps," *Proceedings of the Royal Society of London A*, Vol. 282, No. 1389, 1964, pp. 155–165. doi:10.1098/rspa.1964.0223

[18] Serway, R. A., *Physics for Scientists and Engineers*, 4th ed., Holt, Rinehart, and Winston, New York, 1996.

[19] Hutt, J. J., "A Study of Design Details of Rocket Engine Swirl Injection Elements," Ph.D. Dissertation, Dept. of Mechanical Engineering, Pennsylvania State Univ., University Park, PA, 2000.

D. Talley
Associate Editor